Nuclear Inst. and Methods in Physics Research, A 1014 (2021) 165709

Contents lists available at ScienceDirect

Nuclear Inst. and Methods in Physics Research, A

journal homepage: www.elsevier.com/locate/nima

X-band RF photoinjector design for the CompactLight project

D. González-Iglesias [a,*], A. Aksoy [b], D. Esperante [a], B. Gimeno [a], A. Latina [c], M. Boronat [a], C. Blanch [a], N. Fuster-Martínez [a], P. Martinez-Reviriego [a], P. Martín-Luna [a], J. Fuster [a]

[a] Instituto de Física Corpuscular (IFIC), University of Valencia-Consejo Superior de Investigaciones Científicas, Calle Catedrático José Beltrán, 2, 46980 Paterna, Valencia, Spain
[b] Institute of Accelerator Technologies, University of Ankara, Bahçelievler, Örencik Serpme Evler No:26, 06830 Gölbaşı/Ankara, Turkey
[c] European Organization for Nuclear Research (CERN), CH-1211, Genève 23, Geneva, Switzerland

ARTICLE INFO

Keywords:
Photoinjector
X-band
Electron sources
Free electron laser
Beam generation

ABSTRACT

RF photoinjectors have been under development for several decades to provide the high-brightness electron beams required for X-ray Free Electron Lasers. This paper proposes a photoinjector design that meets the Horizon 2020 CompactLight design study requirements. It consists of a 5.6-cell, X-band (12 GHz) RF gun, an emittance-compensating solenoid and two X-band traveling-wave structures that accelerate the beam out of the space-charge-dominated regime. The RF gun is intended to operate with a cathode gradient of 200 MV/m, and the TW structures at a gradient of 65 MV/m. The shape of the gun cavity cells was optimized to reduce the peak electric surface field. An assessment of the gun RF breakdown likelihood is presented as is a multipacting analysis for the gun coaxial coupler. RF pulse heating on the gun inner surfaces is also evaluated and beam dynamics simulations of the 100 MeV photoinjector are summarized.

1. Introduction

Low emittance, high brightness electron sources are a key component of X-ray Free Electron Lasers [1]. The electron source is typically a photoinjector that consists of an RF gun followed by accelerator structures. The electron bunch is generated by illuminating the gun photocathode with short laser pulses. Acceleration in the gun needs to occur rapidly to mitigate space charge effects so high cathode gradients are required. Also, the gun is typically surrounded by a solenoid magnet to reduce the beam emittance increase that occurs in the early stages of acceleration [2].

In this paper, we present a design of an RF photoinjector that meets the requirements of the CompactLight project (XLS), which are summarized in Table 1 [3]. Briefly, CompactLight was a H2020 Design Study funded by the European Union between January 2018 and January 2021. Launched by a group of 22 International Laboratories and two companies, its goal was to expand the use of FEL light sources globally by bringing together recent advances in FEL sub-systems – i.e., electron photoinjectors, linac accelerator structures and undulators – to create a next-generation facility design that is significantly lower in cost and size than existing facilities.

Our proposed RF photoinjector is based on a 5.6-cell, X-band (12 GHz) RF gun that is intended to operate with a 200 MV/m cathode gradient. The goal is to generate low emittance, high peak current bunches (one per pulse) with a final kinetic energy near 100 MeV. The injector would be employed to drive an X-ray Free Electron Laser after further beam acceleration. The photoinjector also includes a solenoid magnet to compensate space-charge induced beam emittance growth, and two RF acceleration sections to achieve a beam energy near 100 MeV. The photoinjector layout is shown in Fig. 1.

The design is similar to the SLAC X-band (11.4 GHz) photoinjector, which includes a 5.5 cell gun that operates with a cathode gradient up to 200 MV/m [4]. However, the SLAC gun design uses a dual feed racetrack coupler to eliminate the coupler RF dipole and quadrupole RF fields, while our design employs a coaxial coupler that naturally preserves the axial symmetry of the gun to avoid the RF field distortions that degrade the beam emittance. In addition, this design choice allows more space for the solenoid magnet, which might relax manufacturing tolerance requirements. The coaxial coupler is more prone to multipactoring, but the solenoid field helps suppress it.

The main design parameters of the proposed gun are summarized in Table 2 and are discussed in later sections of the paper. The bulk of the gun will be made of copper.

In this paper, we first describe the electromagnetic design of the 5.6-cell RF gun cavity and then discuss in detail operational aspects that will impact its performance. These include the multipactoring susceptibility of the coaxial coupler, which is assessed by means of numerical simulations. In addition, the RF breakdown likelihood is estimated and the temperature rise on the gun inner surfaces from RF pulse heating is evaluated. The RF power system layout required to

* Corresponding author.
E-mail address: daniel.gonzalez-iglesias@uv.es (D. González-Iglesias).

https://doi.org/10.1016/j.nima.2021.165709
Received 14 January 2021; Received in revised form 26 July 2021; Accepted 26 July 2021
Available online 5 August 2021

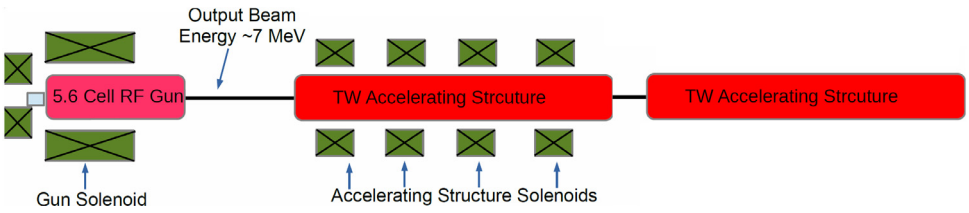

Fig. 1. RF photoinjector layout. After the 5.6-cell RF gun, two identical TW accelerator structures are used to increase the beam energy to 100 MeV.

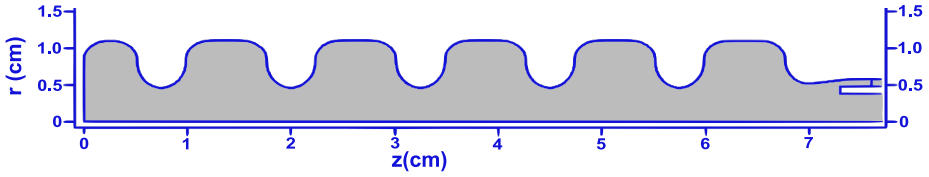

Fig. 2. Cross section of the axial symmetric, 5.6 cell RF gun with a coaxial coupler.

Table 1
CompactLight goal parameters for the photoinjector.

Parameter	Unit	Value
Charge, Q	pC	75
Bunch Length, σ_z	fs	350
Energy spread, $\Delta E/E_{avg}$	(%)	0.5
Peak current	A	60
rms norm. emittance, ϵ_x	mm mrad	0.2
Pulse repetition rate, f_p	kHz	0.1–1.0

Table 2
Main parameters of the RF gun.

Parameter	Unit	Value
Frequency f_π	GHz	11.994
RF Electric Cathode field	MV/m	200
Maximum surface RF electric field (for 1 MV/m at cathode)	MV/m	0.998
Coupling factor, β		1.008
Mode separation, Δf	MHz	27.1
Filling time, τ	ns	112.5
Required magnetic field to suppress multipactor	mT	360
Breakdown Rate, BDR (for pulse of 286 ns)	bpp/m	2.6×10^{-6}
Pulse heating (for pulse of 286 ns), ΔT	°C	26.5

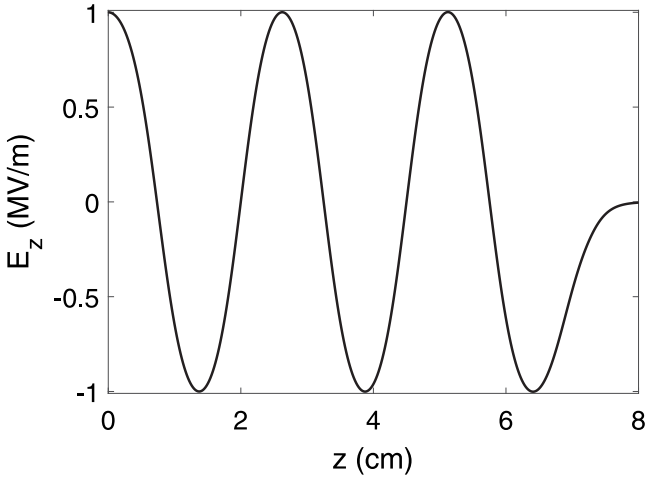

Fig. 3. RF electric field along the axis of the RF gun, normalized to 1 MV/m at the cathode.

feed the photoinjector is then outlined, and finally the beam dynamics simulations that have been performed are summarized.

2. Electromagnetic design of the RF gun

The cross section of RF gun geometry is shown in Fig. 2. It consists of six coupled cells, five with length $\lambda/2$ where λ is the free-space RF wavelength, and one (first cell) with length 0.6 $\lambda/2$. The first cell length was chosen based on beam emittance optimization studies similar to those discussed in Ref. [5]. The cells are coupled by means of elliptical irises instead of circular ones to reduce the peak iris electric field [6,7], which should reduce the likelihood of RF breakdown. The gun will be powered via a rectangular WR90 waveguide, which will connect to the gun coaxial section via a door-knob-like geometry (not shown in Fig. 2) [8]. Ignoring this transition, the gun is axisymmetric, allowing the use of the 2D eigenmode solver SUPERFISH [9] to optimize the design. SUPERFISH has the advantage of being much faster than 3D codes.

The electromagnetic design of the RF gun was carried out in two steps. In the first step, the RF gun was divided in three parts: the first (cathode) cell, the central cells and the last cell with the coaxial coupler. For each part, a separate optimization was performed to achieve the goal parameters. Specifically, each part was tuned to the desired operating RF frequency and the shape of the cells was varied to minimize the surface RF electric field for a given cathode field. The output cell was matched with the coaxial coupler to obtain the desired coupling factor β. Also, an effort was made to maximize the frequency separation between the operating π-mode and the nearest-neighbor mode to avoid its excitation during RF transients [10].

In the second design step, the three tuned parts were merged to form the 5.6 cell RF gun cavity. The resulting device was re-optimized to achieve equal peak axial fields in the cells. The electromagnetic design optimization tasks were carried out using a multidimensional Newton–Raphson algorithm that allows one to find a simultaneous solution for a set of p non-linear equations that depend on k independent variables [11]. In this case, the p non-linear equations represent the performance parameters of the gun, which are intended to match to specific values (i.e., frequency, coupling factor, etc.), while the k independent variables are those gun dimensions to be optimized.

The gun π-mode frequency was chosen to be 11.994 GHz, which is typically used in Europe for X-band structures. The coupling factor goal was $\beta = 1$ to minimize RF reflections from the cavity. Fig. 3 shows the resulting RF electric field along the gun axis. The maximum electric field values in the cells are equal to better than 1%. In Fig. 4, the surface electric field along the wall contour of the gun is shown.

For a 1 MV/m cathode field, the maximum surface electric field is 0.998 MV/m. Other relevant gun parameters are the coupling factor,

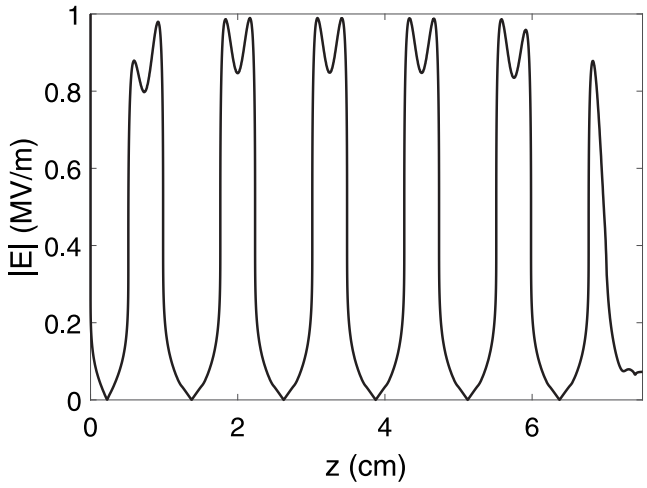

Fig. 4. Surface RF electric field as a function of the axial position for a 1 MV/m cathode gradient.

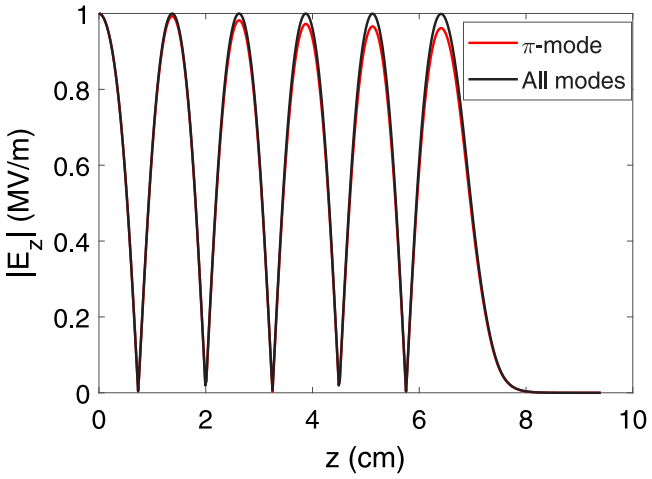

Fig. 5. RF electric field along the axis of the RF gun, normalized to 1 MV/m at the cathode. Results are presented for two cases: considering only the presence of the π-mode, and taking into account all the possible excited modes in the gun cavity.

$\beta = 1.005$, the separation between the π-mode and the nearest neighboring mode, $\Delta f = 27.1$ MHz, and the cavity fill time, $\tau = 112.5$ ns. In addition, the effect of the neighboring modes on the RF electromagnetic field pattern of the gun was analyzed by using an equivalent circuital model and following a procedure similar to that described in Appendix A of [10]. A small deviation in the steady-state RF electric field was found when comparing the on-axis E_z field for just the π-mode with that including all modes: Fig. 5 compares these profiles. To eliminate this field difference, the initial gun design was re-optimized taking into account the presence of the neighboring modes, which did not appreciably change the aforementioned gun parameters.

After re-optimization, the maximum on-axis steady-state electric field, including the contribution from all modes, is the same for all cells as can be seen from the red curve in Fig. 6. These results, obtained with SUPERFISH in combination with the circuit model, were benchmarked at the design frequency with the 3D numerical electromagnetic field solver HFSS [12], which also accounts for power attenuation along the structure. The steady-state HFSS result is also plotted in Fig. 6, and agrees well with our 2D model, thus validating our design approach.

Table 3
Properties of the TW accelerating sections.

Parameter	Unit	Value
Frequency	GHz	11.994
Average gradient	MV/m	65
Total length	m	0.9
Number of cells		108
Phase advance per cell	rad	$\frac{2\pi}{3}$

Table 4
Multipactor susceptibility windows for the coaxial coupler. P is the power flow in the coaxial waveguide and V is the peak voltage between the inner and outer conductor.

Multipactor window	P (MW)	V (kV)
1	0.035–0.56	0.891–3.565
2	1.20–3.10	5.219–8.388

3. TW accelerating structures

The two traveling wave (TW) structures downstream of the gun also operate at 12 GHz. The structure design chosen is that developed in the framework of the CompactLight project [13]. The main parameters of these TW accelerator structures are summarized in Table 3.

4. Multipactor analysis in the coaxial coupler

The multipactor phenomenon is an electron avalanche-like discharge occurring in RF components operating under vacuum [14]. The motion of free electrons can synchronize with the RF electric field and release secondary electrons each time they impact the cavity wall. This process can lead to an exponential increase of the electron population, which discharges the stored RF energy in the cavity.

For the coaxial coupler, a set of multipactor numerical simulations were performed at different RF power levels to determine the multipactor susceptibility zones in which exponential growth is expected to occur. These simulations were carried out with a 3-D tracking code that was developed in-house. It uses the Monte Carlo method and a model in which the motion of groups of electrons (i.e., an 'effective' electron) are governed by the electromagnetic field [15]. The trajectory of an effective electron is found numerically by solving its equation of motion by means of the Velocity-Verlet algorithm. Each effective electron evolves in time, eventually colliding with the metallic walls of the inner and outer coaxial conductors. The Secondary Electron Yield (SEY) after each impact is evaluated as a function of the impact kinetic energy and impinging angle using the SEY model formulated in [15]. The secondary electrons are then re-emitted from the impact location with a random initial velocity given by a Maxwellian distribution with an average energy of a few eV (typically $\approx$ 4 eV). The driving electromagnetic field experienced by each effective electron is that corresponding to the fundamental TEM mode of the coaxial guide at the gun RF frequency. The evolution of the electron population is plotted as a function of the time, and if an exponential increase is observed, it is assumed that a multipactor discharge would occur. Fig. 7 shows an example output of the multipactor simulator for a case where the population exponentiates. The simulations show there are two multipactor bands within the gun operating range, which are listed in Table 4.

At the RF power level required to achieve the nominal gun gradient, the RF voltage in the coaxial line is 13.2 kV, which is above the second multipactor window, and hence no multipactor discharge is expected. However, when the RF power is turned on, there will be a transient increase in the RF field in both the coaxial line and gun cavity. The RF voltage envelope in the coaxial line can be well approximated by [16]:

$$V(t) = \begin{cases} V_0 \left(1 - e^{-\frac{t}{\tau}}\right) & 0 \le t \le t_{\text{on}}, \\ V_0 \left(1 - e^{-\frac{t_{\text{on}}}{\tau}}\right) e^{-\frac{t - t_{\text{on}}}{\tau}} & t > t_{\text{on}}, \end{cases} \quad (1)$$

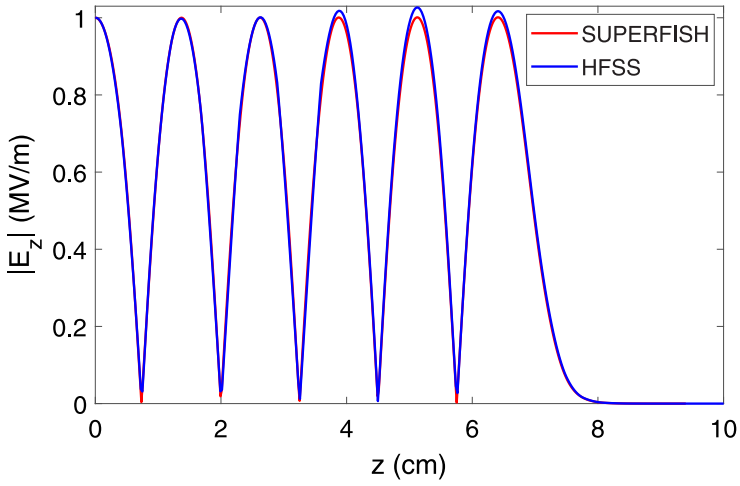

Fig. 6. RF electric field along the axis of the RF gun, normalized to 1 MV/m at the cathode, computed with SUPERFISH plus a circuit model for the neighboring modes (red curve), and with HFSS (blue curve). (For interpretation of the references to color in this figure legend, the reader is referred to the web version of this article.)

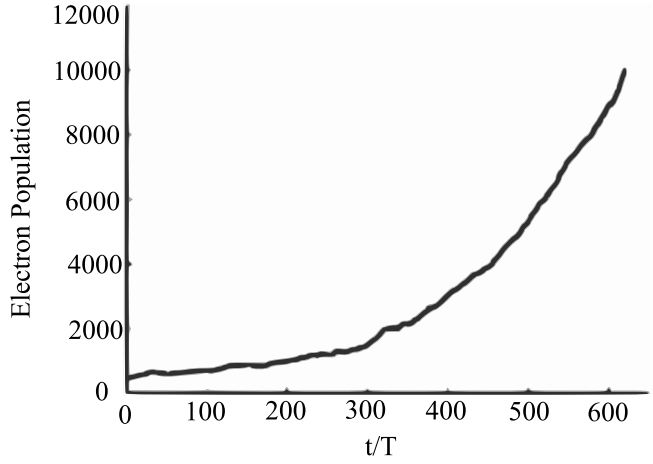

Fig. 7. Electron population inside the coaxial coupler as a function of time in units of the RF period (T) for a case where a multipactor discharge is expected to occur.

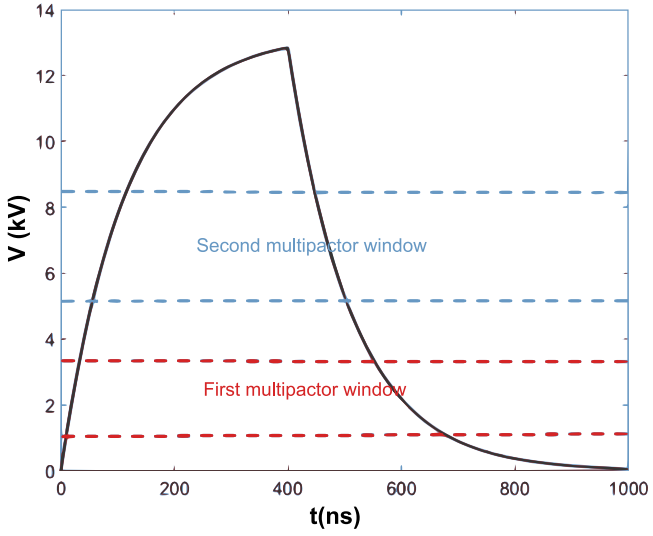

Fig. 8. RF Voltage envelope in the coaxial section during the RF pulse. The two multipactor windows are indicated by dashed lines.

where V_0 is the RF voltage in steady state, t_{on} is the RF pulse duration, t is time, and τ is the filling time. Fig. 8 shows the RF voltage envelope amplitude in the coaxial coupler for a pulse with $t_{on} = 400$ ns.[1] During the cavity filling, there are two time intervals (15 ns and 23 ns durations) in which multipactor discharges are expected to occur — they correspond to the first and second window, respectively. Similarly, mulipactoring is expected to appear during the emptying of the cavity in two time intervals (53 ns and 156 ns durations).

Despite the multipactor risk, it does not represent an insurmountable problem since it can be suppressed by means of an external magnetic field. This method was experimentally demonstrated for a coaxial line in Ref. [17], which gives two requirements regarding its application. The first is that the magnetic field is applied along the coaxial waveguide axis. The second is that the field strength is greater than the value obtained by equating the RF frequency to the electron cyclotron frequency, that is:

$$B_{dc,min} = \frac{m}{e} 2\pi f$$

where m and e are the mass and charge of the electron, respectively. Given the gun operating frequency, the minimum required field is 428.5 mT.

To confirm this prediction, additional multipactor numerical simulations were performed that included the presence of a static axial magnetic field. The results showed that no multipactor discharge is expected when the minimum required external magnetic field is applied. Moreover, a static magnetic field of only 360 mT was required to suppress the discharge. Accordingly, a solenoid with such magnetic field value (and higher) is included in the RF photoinjector layout for multipactor mitigation, as well as for beam emittance compensation, which is discussed in Section 9.

5. RF breakdown risk

RF breakdown is a phenomenon that occurs at high electric surface field [18]. During breakdown, an electric current is emitted from the walls of the device, forming a plasma that causes a significant RF mismatch and a sudden increase the vacuum pressure level. The risk of RF breakdown is generally characterized by a normalized breakdown rate (BDR), which is defined as the expected number of breakdowns per

[1] The final photoinjector design employs a shorter pulse (286 ns) due to RF power system constraints. However, this fact does not affect the conclusions from this section.

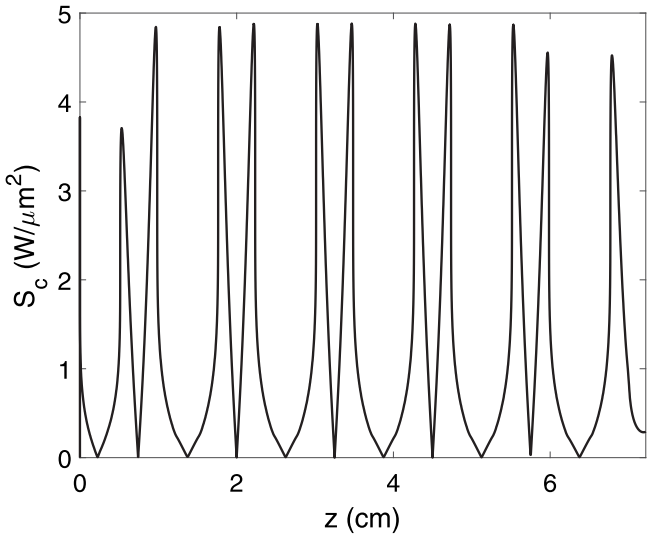

Fig. 9. Modified Poynting vector along the RF gun surface as a function of axial position for a 200 MV/m cathode gradient.

pulse and per meter length of the structure. According to Ref. [19], the BDR can be roughly estimated based on the maximum of a modified Poynting vector, S_c that is computed along the structure surfaces. The modified Poynting vector is defined in terms of the complex Poynting vector $\vec{S}$ as follows:

$$S_c = \left\| \mathrm{Re}\,\vec{S} \right\| + g_c \left\| \mathrm{Im}\,\vec{S} \right\|, \qquad \vec{S} = \frac{1}{2}\vec{E} \times \vec{H}^*$$

where Re $\vec{S}$ and Im $\vec{S}$ are the real and the imaginary parts of the complex Poynting vector $\vec{S}$, respectively, $\vec{E}$ and $\vec{H}^*$ are the electric and conjugate complex magnetic field phasors, respectively, and g_c is an empirical parameter that ranges from 0.15 to 0.2, but a value of 1/6 is typically used. Fig. 9 is a plot of the modified Poynting vector along the gun surface assuming a 200 MV/m cathode field. The maximum value of S_c for the RF gun is 4.88 W/μm^2. The relation among the modified Poynting vector, BDR and the RF pulse length, t_{on}, is given by the empirical expression,

$$BDR = \frac{S_c^{15} t_{\mathrm{on}}^5}{C} \tag{2}$$

where C a constant, which using measured breakdown rate data provided in Ref. [19], is $C = 9.8 \times 10^{27}$ W^{15}ns$^5\mu$ m^{-30}bpp^{-1}m. The above expression allows one to estimate the BDR during a period when the gradient is constant. However, this is not the case for the RF gun where the gradient varies during the fill and discharge. As a result, the modified Poynting vector will vary with time, which must be considered to properly estimate the BDR. To do this, one notes that the modified Poynting vector is proportional to the square of the RF electric field, which is well approximated by Eq. (1). The BDR is then calculated by splitting the pulse into the sum of many short pulses, assuming that for each of them, the corresponding BDR is given by incremental change in Eq. (2) [20]:

$$\mathrm{BDR}_{pulse} = \frac{1}{C} \lim_{n\to\infty} \sum_{k=1}^{n} S_c^{15}(t_k)\left(t_{k+1}^5 - t_k^5\right) = \frac{5}{C}\int_0^{T_p} S_c^{15}(t)\, t^4 dt \tag{3}$$

where $T_p = nt_p$ is the total pulse length, n is the number of short pulses in which total pulse length is divided and t_p is the length of each of the short pulses.

Fig. 10 shows the resulting BDR in the RF gun as a function of the pulse length. The BDR predictions corresponding to the constant gradient case are included for comparison. There is a significant difference between the two curves, which shows the importance to taking into consideration the transient effect. For $t_{\mathrm{on}} \gg \tau$, the transient result approaches that of the constant gradient case as expected.

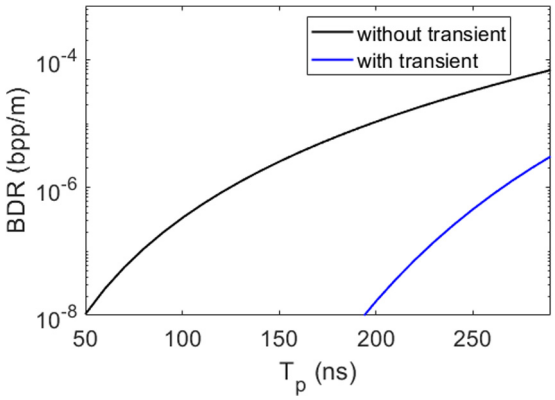

Fig. 10. Estimated BDR in the gun as a function of RF pulse length for a steady state cathode gradient of 200 MV/m. The blue curve accounts for the transient change in the field while the black curve assumes a constant field equal to the steady state value. (For interpretation of the references to color in this figure legend, the reader is referred to the web version of this article.)

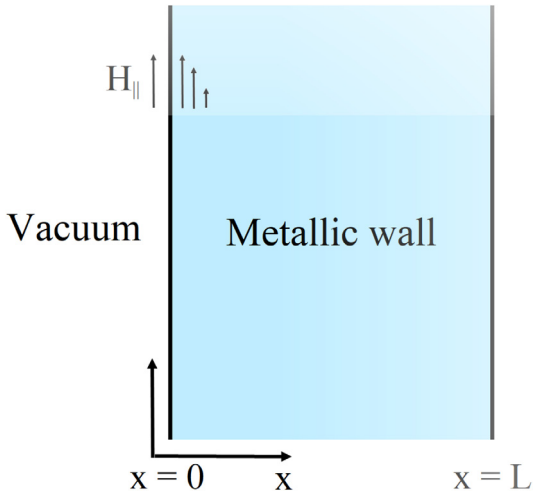

Fig. 11. Model of the gun inner wall used to compute pulse heating.

6. RF pulse heating

The surface currents associated with the RF fields in a structure induce ohmic losses on the walls that increase the metal temperature. Pulsed temperature increases over about 50° are known significantly increase the BDR in copper structures from the fatigue related surface damage it causes [21]. Thus one wants to avoid operating at gradients and pulse lengths that produce such peak temperature rises.

The temperature increase during the RF pulse in the gun can be estimated by means of a 1D model that analytically solves the heat transfer differential equation for a metallic wall of thickness L. Fig. 11 shows the geometry assumed in the 1D model. The left boundary of the wall corresponds to the inner vacuum side of the device where the RF electromagnetic fields are present. Both wall boundaries (left and right sides) are assumed to be thermally isolated. Given these assumptions, the 1D heat transfer equation can be solved analytically following a procedure similar to that described in Ref. [22] and [20]. For our calculations, the equations given in Ref. [20] are employed since they take into account the temporal variation of the surface field. The resulting time dependent temperature profile within the metallic wall is given by:

$$\Delta T(x,t) = u_0(t) + \sum_{n=1}^{\infty} u_n(t)\cos\left(\frac{\pi n x}{L}\right), \quad 0 \le t \le t_{\mathrm{on}} \tag{4}$$

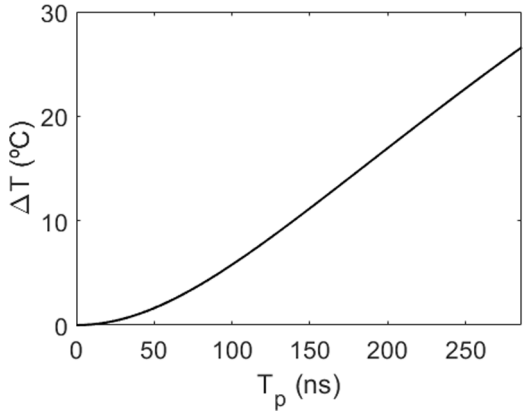

Fig. 12. Maximum pulse temperature increase in the RF gun copper walls as a function of pulse length for a steady state cathode electric field of 200 MV/m.

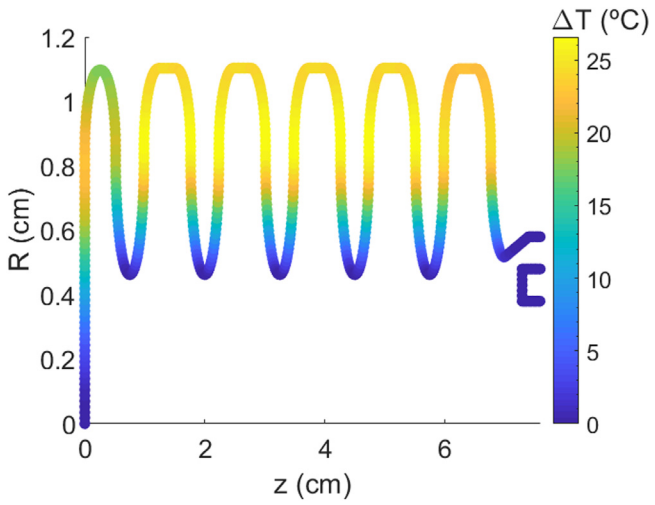

Fig. 13. Maximum pulse temperature increase on the RF gun copper surface for $T_p = 286$ ns and steady-state cathode field of 200 MV/m.

with

$$u_0(t) = \frac{g_0}{2}\left[t + \tau\left(2e^{-\frac{t}{\tau}} - \frac{1}{2}e^{-\frac{2t}{\tau}} - \frac{3}{2}\right)\right], \tag{5}$$

$$u_n(t) = \frac{g_n}{\left(\frac{\pi Dn}{L}\right)^2}\left(1 - e^{-\left(\frac{\pi Dn}{L}\right)^2 t}\right) + \frac{g_n}{\left(\frac{\pi Dn}{L}\right)^2 - \frac{2}{\tau}}\left(e^{-\frac{2t}{\tau}} - e^{-\left(\frac{\pi Dn}{L}\right)^2 t}\right) + \frac{2g_n}{\left(\frac{\pi Dn}{L}\right)^2 - \frac{1}{\tau}}\left(e^{-\left(\frac{\pi Dn}{L}\right)^2 t} - e^{-\frac{t}{\tau}} - \right),$$

and

$$g_0 = \frac{2\alpha}{L}\left(1 - e^{-\frac{2L}{\delta}}\right),$$

$$g_n = \frac{8\alpha L}{4L^2 + \pi^2\delta^2 n^2}\left(1 - e^{-\frac{2L}{\delta}}(-1)^n\right), \tag{6}$$

$$\alpha = \frac{R_s|H_{\|,0}|^2}{2\rho C_e}, \quad D = \sqrt{\frac{\kappa}{\rho C_e}};$$

where $\delta = \sqrt{\frac{2}{\sigma\mu_0\omega}}$ is the skin depth, $R_s = 1/(\delta\sigma)$ is the surface resistance, μ_0 is the vacuum permeability, $\omega = 2\pi f$ is the angular frequency, κ is the thermal conductivity, ρ is the density, and C_e is the specific heat.

Using this equation, the resulting maximum pulse temperature rise on the gun walls as a function of the RF pulse length is shown in Fig. 12, and Fig. 13 shows a color map of the peak temperature rise in the gun for $T_p = 286$ ns. For this pulse length, the maximum temperature rise is $\Delta T = 26.5°$ C, which is below the 50° C limit.

7. RF power system

To achieve a 200 MV/m cathode gradient in steady state, the input RF power at the coaxial coupler port needs to be 11.6 MW. We initially considered using an RF pulse length of 400 ns (i.e., 3.6 fill times), which ensures that the field rises to within 3% of this value. During the fill period, there is a significant amount of RF power reflected towards the RF source, which will be a klystron. Using a circulator to protect the klystron is not an option as X-band circulators at the required power level are not available. As a consequence, one must add enough delay line between the klystron and gun so the reflected power arrives at the klystron when it is no longer producing power.

For the delay line, we will use circular waveguide with a radius of 1.905 cm operating in the low-loss TE_{01} mode. A mode converter similar to that described in Ref. [23] will be employed to change from the rectangular TE_{01} mode at the klystron output to the circular TE_{01} mode.

For the RF system layout, several options based on different klystron models were explored, and the scheme chosen is shown in Fig. 14. It is based on a Toshiba E37113 klystron with an RF peak power of 6 MW, a pulse length of up to 5 μ s, and maximum pulse repetition rate of 400 Hz. To achieve an input power at the gun entrance of at least 11.6 MW, we will use a SLED-II pulse compression scheme similar to that employed in the Xbox 3 facility at CERN [24] where the flattop output power can be enhanced by a factor of 3.5 in a reduced pulse length of 300 ns. With a pulse compression factor of only 3, we will be able to provide 18 MW peak power, which is more than needed. However, the resulting 300 ns pulse is shorter than the desired pulse length of 400 ns. To compensate, we will excite the gun with a step-like RF pulse [10] whose profile is shown in the left side of Fig. 15.

During the initial portion of the RF pulse ($t < t_h$), the power is ΛP_{in} where P_{in} is the power required to achieve a 200 MV/m cathode gradient in steady state. We chose $\Lambda = 1.2$ ($\Lambda P_{in} = 13.9$ MW) and $t_h = 271.8$ ns, for which the resulting cathode gradient versus time is shown in the right side of Fig. 15. For a laser injection time of $t_{inj} = 276$ ns, the axial E_z profile matches well the steady state case. With this scheme, a circular waveguide delay line length of $L = 25.7$ m is needed to protect the klystron, and accounting for transport losses, the delay line input power needs to be 15.5 MW.

8. Beam emittance solenoid

A schematic view of the solenoid that will be used for beam emittance compensation is shown in Fig. 16. It was designed using the Poisson code [25] and consists of two coils that are each surrounded by a ferromagnetic yoke made of a low carbon steel with a relative magnetic permittivity of 250. The current in the two coils would have opposite polarities to zero the field at the cathode and thus avoid increasing the initial beam emittance. Fig. 16 also shows the axial magnetic field profile. The inner coil radius (r_c) is 4 cm, and to generate a peak axial field of 0.5 T, a current of 165 A is required in the downstream coil.

9. Photoinjector beam dynamics

Beam simulations of the photoinjector have been carried out using the codes GPT [26], ASTRA [27] and RF-Track [28]. We employed 20,000 macro-particles to simulate a 75 pC bunch charge that is excited

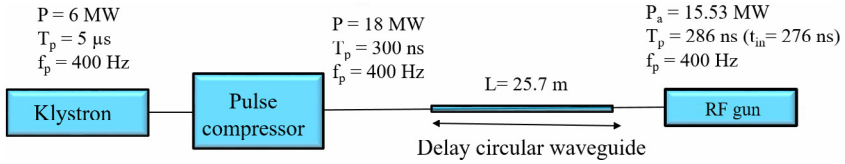

Fig. 14. RF power system layout for the photoinjector. Note that P_a is the RF power at the entrance of the delay line that is required to achieve a cathode gradient of 200 MV/m.

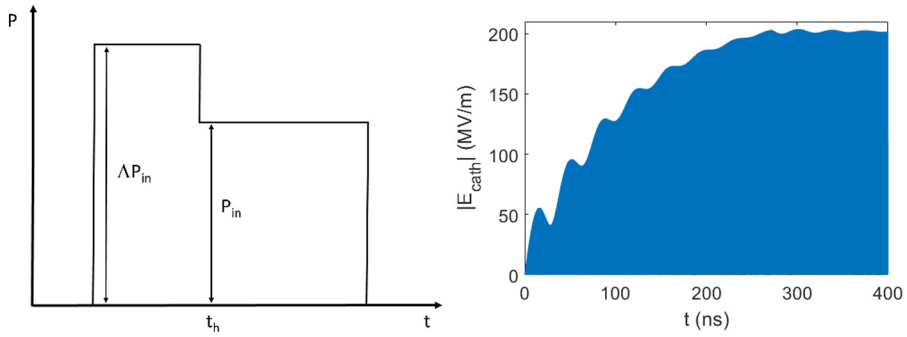

Fig. 15. Left: profile of the step-square RF pulse. Right: RF electric field amplitude at cathode as a function of time for the step-square pulse.

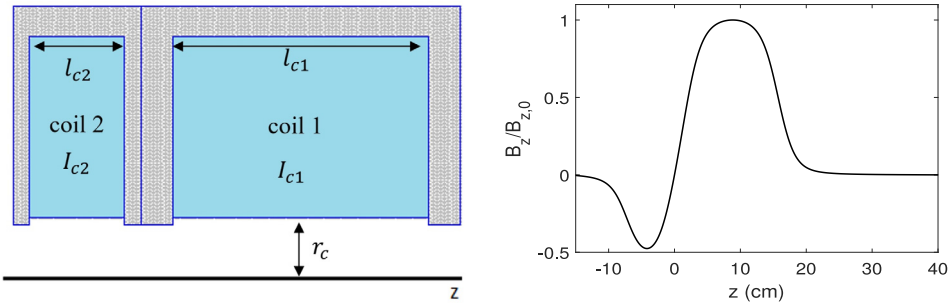

Fig. 16. Left: schematic of the solenoid used for the beam emittance compensation. Right: normalized magnetic field along the axis of the solenoid.

by a 0.3 ps long, flat laser pulse with a 0.25 mm rms transverse width. Given these laser pulse parameters and a 200 MV/m cathode gradient, the transverse intrinsic emittance, in case of a copper cathode, is about 0.12 mm mrad [29]. We also assumed that the particles emerging from the cathode at room temperature have a kinetic energy of $E_k = 0.05$ eV.

The bunch phase, solenoid strength, accelerator TW phase, and the spacing between the gun and first TW structure were varied to achieve the lowest emittance. In particular, different combinations of the above parameters were tried to find an optimum working point. The spacing between the gun and first accelerator structure were chosen according to Ferrario's criterion [30]. It states that the minimum emittance at the end of the first accelerator structure occurs when the beam size is minimum at the entrance to this structure. Using the code GPT, an optimum set of parameters was found that produced a minimum projected emittance at the end of the first TW structure.

9.1. Codes comparison

The results from the GPT simulations were benchmarked with the codes ASTRA and RF-Track. Comparisons of bunch energy and bunch length along the injector are shown in Fig. 17. Likewise, the evolution of the rms emittance and transverse beam size are compared in Fig. 18 and Fig. 19. Finally, transverse and longitudinal phase space plots of the bunch at the end of the second TW structure are compared in Fig. 20.

The simulations with GPT were carried out using a 2D map for the RF field of the gun and a 1D map for the TW accelerator structure fields. For the simulations with ASTRA and RF-Track, 1D maps for both the gun and the TW accelerator structures were employed.

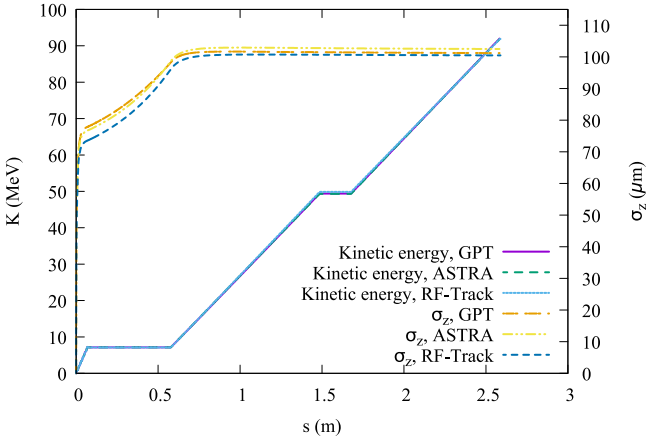

Fig. 17. Energy gain and bunch length evolution along the injector.

The tracking results agree fairly well even though the codes differ in many respects: they use different methods to interpolate the electromagnetic fields, they use different algorithms to integrate the equations of motion, and most likely, they have different space-charge algorithms. The beam properties at the end of the second TW structure that were obtained with each code are listed in Table 5. The rms emittances are about 0.2 mm·mrad, which meets the design goal.

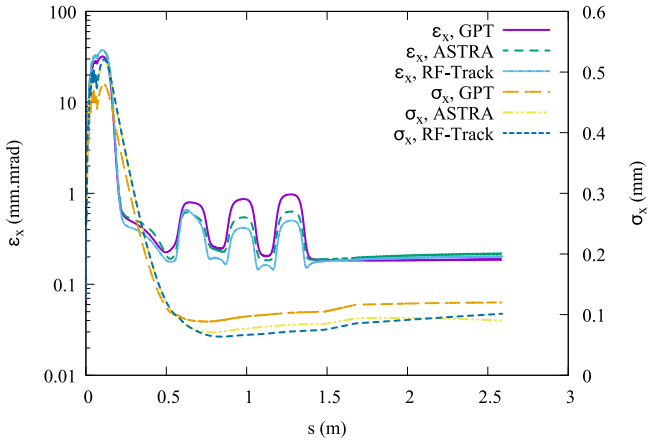

Fig. 18. Projected normalized horizontal emittance and transverse RMS beam size along the injector.

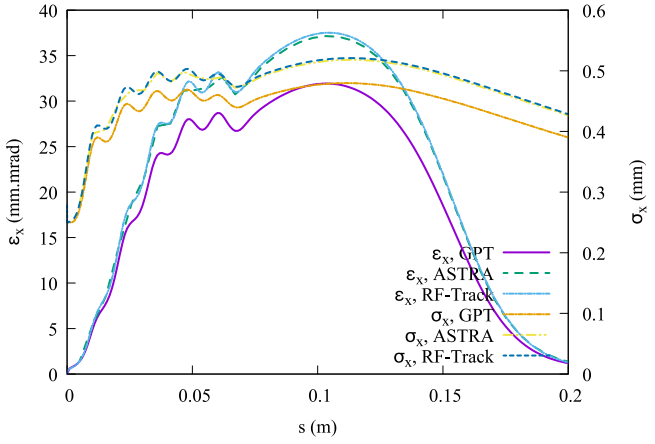

Fig. 19. Projected normalized horizontal emittance and transverse RMS beam size within 20 cm of the cathode.

Table 5
Electron beam properties at the end of the photoinjector.

Parameter	GPT	ASTRA	RF-Track
Kinetic energy (MeV)	91.9	91.8	91.9
Bunch length (fs)	338	341	335
Energy spread (%)	0.46	0.50	0.43
Peak current (A)	64	64	64.6
RMS norm. emittance (mm mrad)	0.20	0.21	0.20
Transverse size (mm)	0.12	0.09	0.10

9.2. Solenoid misalignment studies

The beam emittance is particularly sensitive to the misalignment of the gun solenoid magnet. Such a misalignment causes the electron beam to follow the magnetic axis, sending the beam off-axis. These excursions can be easily removed using dipole corrector magnets; however, we did not assume this as a worst case.

We used RF-Track for the misalignment study and varied the horizontal angle of the solenoid magnet relative to the accelerator axis. We focused on two quantities: the average beam offset along the injector and the beam emittance at the end of the second traveling wave structure. The simulation also included wakefield effects in the traveling wave structures. As shown in Fig. 21, the emittance growth is negligible (< 1.5%) for misalignment angles up to 200 mm·mrad.

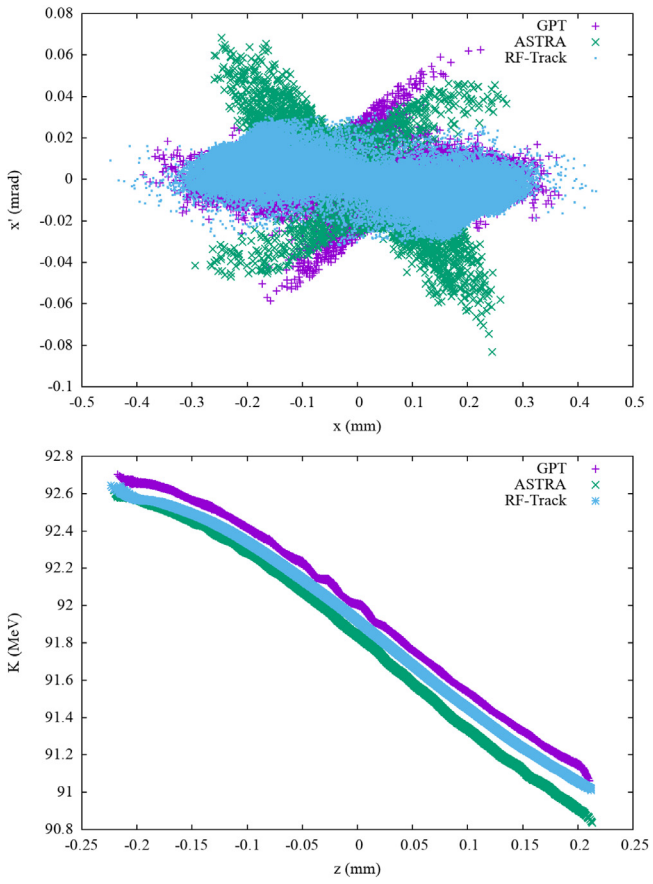

Fig. 20. Transverse and longitudinal phase space plots of the bunch at the end of the second TW structure.

10. Conclusions

The design of a compact (2.6 m long) X-band RF photoinjector for the CompactLight project was presented. It is based on a 5.6-cell, 12 GHz, RF gun that would operate with a 200 MV/m cathode gradient. An estimate of the gun RF breakdown rate found it was at the one in a million pulse level, and an analysis of the multipactor risk in the coaxial coupler showed that the magnetic field from the emittance compensation solenoid would suppress it. The temperature increase along the RF gun walls due to the RF pulse heating was found to be below the fatigue damage limit.

Beam dynamics simulations showed that for a bunch charge of 75 pC, an rms normalized emittance of about 0.20 mm·mrad at 90 MeV can be achieved, which meets specifications.

Future studies will consider the generation and transport of dark current, which can likely be suppressed with cathode surface treatments [31], RF conditioning and collimation.

CRediT authorship contribution statement

D. González-Iglesias: Software, Writing, Investigation, Methodology. **A. Aksoy:** Supervision, Conceptualization, Methodology, Software. **D. Esperante:** Supervision, Conceptualization, Methodology, Funding acquisition. **B. Gimeno:** Supervision, Conceptualization, Methodology, Funding acquisition. **A. Latina:** Supervision, Conceptualization, Methodology, Writing, Software. **M. Boronat:** Supervision. **C. Blanch:** Supervision. **N. Fuster-Martínez:** Supervision. **P. Martinez-Reviriego:** Supervision. **P. Martín-Luna:** Supervision. **J. Fuster:** Supervision, Funding acquisition.

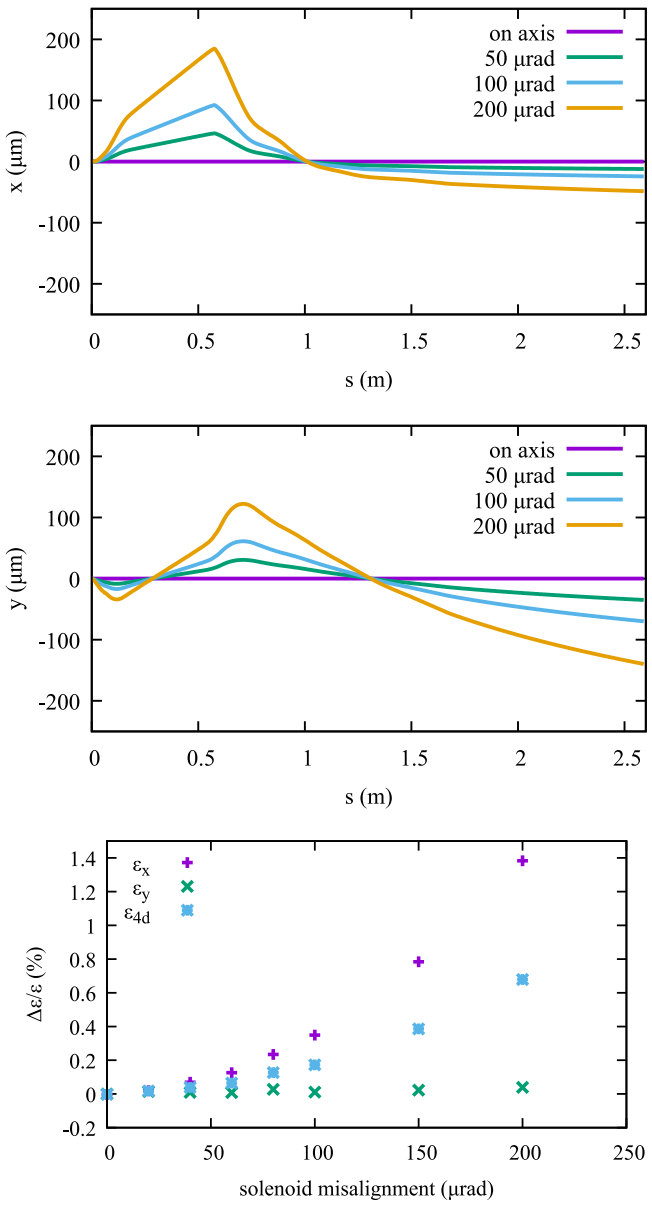

Fig. 21. Impact of angular solenoid misalignments. The two top plots show the beam orbit along the injector for different misalignment angles. The bottom plot shows the emittance growth at end of the injector due to the bunch deflections.

Declaration of competing interest

The authors declare that they have no known competing financial interests or personal relationships that could have appeared to influence the work reported in this paper.

Acknowledgments

This work was supported by the European Union's Horizon 2020 research and innovation program under the grant agreement No 777431 (XLS CompactLight). This research was also supported by the Valencian Regional Government VALi+D postdoctoral grant (APOSTD/2019/155)

The authors would like to thank Igor Syratchev (CERN) and David Alesini (INFN) for their technical advice.

References

[1] E. Jaeschke, S. Khan, J. Schneider, J. Hastings, Synchrotron Light Sources and Free-Electron Lasers: Accelerator Physics, Instrumentation and Science Applications, 2016, pp. 1–1840, https://doi.org/10.1007/978-3-319-14394-1.

[2] D.H. Dowell, Sources of emittance in RF photocathode injectors:Intrinsic emittance, space chargeforcesdue to non-uniformities, RF and solenoid effects, Tech. Rep., SLAC, 1999, "SLAC-PUB-16895".

[3] XLS-CompactLight Project, URL https://www.compactlight.eu/Main/HomePage.

[4] C. Limborg-Deprey, C. Adolphsen, D. McCormick, M. Dunning, K. Jobe, H. Li, T. Raubenheimer, A. Vrielink, T. Vecchione, F. Wang, S. Weathersby, Performance of a first generation X-band photoelectron rf gun, Phys. Rev. Accel. Beams 19 (2016) 053401, https://doi.org/10.1103/PhysRevAccelBeams.19.053401, URL https://link.aps.org/doi/10.1103/PhysRevAccelBeams.19.053401.

[5] A.E. Vlieks, G. Caryotakis, W.R. Fowkes, E.N. Jongewaard, E.C. Landahl, R. Loewen, N.C. Luhmann, Development of an X-band RF Gun at SLAC, AIP Conf. Proc. 625 (1) (2002) 107–116.

[6] A. Vlieks, V. Dolgashev, S. Tantawi, S. Anderson, F. Hartemann, R. Marsh, X-band RF gun development, in: Proceedings of IPAC'10, Kyoto, Japan, 2010, pp. 3816–3818.

[7] R.A. Marsh, F. Albert, S.G. Anderson, G. Beer, T.S. Chu, R.R. Cross, G.A. Deis, C.A. Ebbers, D.J. Gibson, T.L. Houck, F.V. Hartemann, C.P.J. Barty, A. Candel, E.N. Jongewaard, Z. Li, C. Limborg-Deprey, A.E. Vlieks, F. Wang, J.W. Wang, F. Zhou, C. Adolphsen, T.O. Raubenheimer, Modeling and design of an *X*-band rf photoinjector, Phys. Rev. ST Accel. Beams 15 (2012) 102001, https://doi.org/10.1103/PhysRevSTAB.15.102001, URL https://link.aps.org/doi/10.1103/PhysRevSTAB.15.102001.

[8] F.B. Kiewiet, Generation of Ultra-Short, High Brightness Relativistic Electron Bunches (Ph.D. thesi), Technische Universiteit Eindhoven, 2003, https://doi.org/10.6100/IR571240.

[9] K. Halbach, R.F. Holsiger, SUPERFISH - A Computer program for evaluation of RF cavities with cylindrical symmetry, Part. Accel. 7 (1976) 213–222.

[10] D. Alesini, A. Battisti, M. Bellaveglia, F. Cardelli, A. Falone, A. Gallo, V. Lollo, D. Palmer, L. Pellegrino, L. Piersanti, S. Pioli, A. Variola, V. Pettinacci, L. Palumbo, Design, realization, and high power test of high gradient, high repetition rate brazing-free S-band photogun, Phys. Rev. Accel. Beams 21 (2018) 112001.

[11] R. Fletcher, Practical Methods of Optimization, John Wiley & Sons, Ltd, 2013.

[12] Ansys High Frequency Simulation Studio, URL https://www.ansys.com/products/electronics/ansys-hfss.

[13] Courtesy of WP4 team of the XLS-CompactLigth project.

[14] J.R.M. Vaughan, Multipactor, IEEE Trans. Electron Devices 35 (7) (1988) 1172–1180.

[15] A.M. Perez, C. Tienda, C. Vicente, S. Anza, J. Gil, B. Gimeno, V.E. Boria, D. Raboso, Prediction of multipactor breakdown thresholds in coaxial transmission lines for traveling, standing, and mixed waves, IEEE Trans. Plasma Sci. 37 (10) (2009) 2031–2040.

[16] T. Wangler, Principles of RF Linear Accelerators, second ed., John Wiley & Sons, Ltd, 2008.

[17] D. González-Iglesias, A.M. Pérez, S. Anza, J.V. Cardona, B. Gimeno, V.E. Boria, D. Raboso, C. Vicente, J. Gil, F. Caspers, L. Conde, Multipactor mitigation in coaxial lines by means of permanent magnets, IEEE Trans. Electron Devices 61 (12) (2014) 4224–4231.

[18] J. Shao, Investigations on RF Breakdown Phenomenon in High Gradient Accelerating Structures (Ph.D. thesis), Tsinghua U., Beijing, Dept. Eng. Phys., 2016, https://doi.org/10.1007/978-981-10-7926-9.

[19] A. Grudiev, S. Calatroni, W. Wuensch, New local field quantity describing the high gradient limit of accelerating structures, Phys. Rev. ST Accel. Beams 12 (2009) 102001, https://doi.org/10.1103/PhysRevSTAB.12.102001; Phys. Rev. ST Accel. Beams 14 (2011) 099902, (erratum).

[20] D. González-Iglesias, D. Esperante, B. Gimeno, M. Boronat, C. Blanch, J. Fuster, Analytical RF pulse heating analysis for high gradient accelerating structures, IEEE Trans. Nucl. Sci. 68 (2) (2021) 78–91, in press. https://doi.org/10.1109/TNS.2021.3049319.

[21] M. Behtouei, Design and Measurements of the High Gradient Accelerating Structures (Ph.D. thesis), Università di Roma 'La Sapienza', 2019, https://doi.org/10.13140/RG.2.2.16781.90086.

[22] D.P. Pritzkau, RF Pulsed Heating (Ph.D. thesis), Stanford U., 2001.

[23] V.A. Dolgashev, S.G. Tantawi, C.D. Nantista, Design of a compact, multi-megawatt, circular TE(01) mode converter, in: D.K. Abe, G.S. Nusinovich (Eds.), AIP Conf. Proc. 807 (1) (2006) 431–438, https://doi.org/10.1063/1.2158809.

[24] B.J. Woolley, High Power X-band RF Test Stand Development and High Power Testing of the CLIC Crab Cavity (Ph.D. thesis), Lancaster U., 2015.

[25] T. Barts, J. Merson, Users' notes for POISSON/SUPERFISH release 3.0, 1992.

[26] General Particle Tracer, URL http://www.pulsar.nl/gpt/.

[27] A Space Charge Tracking Algorithm (ASTRA), URL https://www.desy.de/~mpyflo/.

[28] A. Latina, RF-Track Reference Manual, Zenodo. https://doi.org/10.5281/zenodo.3887085.

[29] D. Dowell, Sources of Emittance in RF Photocathode Injectors: Intrinsic Emittance, Space Charge Forces Due to Non-Uniformities, RF and Solenoid Effects, Tech. Rep. SLAC-PUB-16895, Stanford University, 2016.

[30] M. Ferrario, J. Clendenin, D. Palmer, J. Rosenzweig, L. Serafini, HOMDYN study for the LCLS RF photoinjector, in: 2nd ICFA Advanced Accelerator Workshop on the Physics of High Brightness Beams, 2000, pp. 534–563.

[31] H. Chen, Y. Du, W. Gai, A. Grudiev, J. Hua, W. Huang, J. Power, E.E. Wisniewski, W. Wuensch, C. Tang, L. Yan, Y. You, Photocathode emission studies: Dark current and schottky-enabled photo-electrons in a high-field RF gun, AIP Conf. Proc. 1507 (2012) https://doi.org/10.1063/1.4773736.